Journal of Solid State Chemistry 246 (2017) 388–398

Contents lists available at ScienceDirect

Journal of Solid State Chemistry

journal homepage: www.elsevier.com/locate/jssc

$K_{1.33}Mn_8O_{16}$ as an electrocatalyst and a cathode

Seifollah Jalili[a,b,*], Elham Moharramzadeh Goliaei[a], Jeremy Schofield[c]

[a] Department of Chemistry, K. N. Toosi University of Technology, P.O. Box 15875-4416, Tehran, Iran
[b] Computational Physical Sciences Research Laboratory, School of Nano-Science, Institute for Research in Fundamental Sciences (IPM), P.O. Box 19395-5531, Tehran, Iran
[c] Chemical Physics Theory Group, Department of Chemistry, University of Toronto, 80 Saint George Street, Toronto, Ontario, Canada M5S 3H6

ARTICLE INFO

Keywords:
Catalytic activity
Thermoelectric properties
Seebeck coefficient
Conductivity
Nanosheet

ABSTRACT

Density functional theory (DFT) calculations are carried out to investigate the electronic, magnetic and thermoelectric properties of bulk and nanosheet $K_{1.33}Mn_8O_{16}$ materials. The catalytic activity and cathodic performance of bulk and nanosheet structures are examined using the Tran-Blaha modified Becke-Johnson (TB-mBJ) exchange potential. Electronic structure calculations reveal an anti-ferromagnetic ground state, with a TB-mMBJ band gap in bulk $K_{1.33}Mn_8O_{16}$ that is in agreement with experimental results. Density of state plots indicate a partial reduction of Mn^{4+} ions to Mn^{3+}, without any obvious sign of Jahn-Teller distortion. Moreover, use of the O *p*-band center as a descriptor of catalytic activity suggests that the nanosheet has enhanced catalytic activity compared to the bulk structure. Thermoelectric parameters such as the Seebeck coefficient, electrical conductivity, and thermal conductivity are also calculated, and it is found that the Seebeck coefficients decrease with increasing temperature. High Seebeck coefficients for both spin-up and spin-down states are found in the nanosheet relative to their value in the bulk $K_{1.33}Mn_8O_{16}$ structure, whereas the electrical and thermal conductivity are reduced relative to the bulk. In addition, figures of merit values are calculated as a function of the chemical potential and it is found that the nanosheet has a figure of merit of ~1 at room temperature, compared to 0.5 for the bulk material. All results suggest that $K_{1.33}Mn_8O_{16}$ nanosheets can be used both as a material in waste heat recovery and as an electrocatalyst in fuel cells and batteries.

1. Introduction

Over the years much effort has been devoted to the identification of a bifunctional electrocatalyst with efficient activity towards both oxygen reduction reactions (ORR) and oxygen evolution reactions (OER) in fuel cells and batteries [1–3]. Two challenging issues to overcome in the development of electrocatalysts are managing the cost of fabrication and reducing the overpotential of the catalyst to improve efficiency. Among the elements of the periodic table, Mn is a low-cost, naturally abundant element, and recent studies suggest that the family of manganese oxides [4] provides the most promising options for ORR and OER. In particular, manganese dioxide (MnO_2) based materials may perform well as electrocatalysts in fuel cells and batteries because of their low cost, environmentally friendly nature [5] and high activity for ORR [6,7]. To stabilize MnO_2 [7] and to enhance activity in OER [8], materials with K^+ intercalated into the MnO_2 structure have been developed. $K_{1.33}Mn_8O_{16}$, with the chemical name Cryptomelane and space group *I4/m*, has a structure similar to that of α-MnO_2 and is a promising candidate as an electrocatalyst and a cathode in Li-ion batteries. It can be used as a cathode because of its unique stability [9] and as an electrocatalyst due to its performance at high temperatures and its low overpotential compared to β-MnO_2 and δ-MnO_2 [10]. In addition to the necessary cathodic behavior, it is essential for $K_{1.33}Mn_8O_{16}$ structures to have thermoelectric features that enable the efficient conversion of heat energy into electric power [11].

Recent research suggests that various crystal structures of $K_{1.33}Mn_8O_{16}$ exhibit different electrocatalyst activity. However there have been no detailed computational studies that examine the effect of crystallite size on the cathodic and electrocatalyst activity of nanostructures relative to bulk structures of $K_{1.33}Mn_8O_{16}$. According to experimental studies, the cathodic and electrocatalytic performance of $K_{1.33}Mn_8O_{16}$ as functional materials requires a large surface area. Nanostructure materials have great potential for catalytic surface reactions because of their large surface area [12,13], making them interesting candidates as materials to be used in the design of many devices. Computational studies of the electronic and the thermoelectric behavior of the nanostructure and bulk structure $K_{1.33}Mn_8O_{16}$ are useful to compare the relative functionality of these materials as

* Corresponding author at: Department of Chemistry, K. N. Toosi University of Technology, P.O. Box 15875-4416, Tehran, Iran.
E-mail address: sjalili@kntu.ac.ir (S. Jalili).

http://dx.doi.org/10.1016/j.jssc.2016.12.009
Received 20 August 2016; Received in revised form 8 December 2016; Accepted 10 December 2016
Available online 12 December 2016

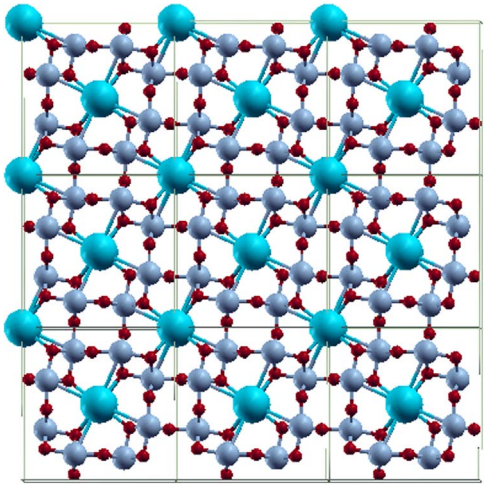

Fig. 1. Schematic image of the optimized unit cells of $K_{1.33}Mn_8O_{16}$. The blue, dark red, and aqua spheres are Mn, O and K atoms, respectively. (For interpretation of the references to color in this figure legend, the reader is referred to the web version of this article).

cathodes and electrocatalysts. Recent experimental studies on α-$K_{0.25}MnO_2$ show that this material has more appropriate sites for the litigation process compared to the unstable structure of α-MnO_2 without K^+ ions, so it can be applied as a cathode material in Li-ion batteries [14]. In addition, the presence of K^+ ions in $K_{0.25}MnO_2$ allows faster ion diffusion in Li-ion batteries [15]. According to theoretical investigations, K^+ doping in α-MnO_2 changes the behavior of this material from semiconductor to metal [16]. Furthermore, based on density functional theory calculations, α-MnO_2 without K^+ ions exhibits antiferromagnetic behavior [17,18]. However, according to the experimental results, in the presence of K^+ ions lower and above 12%, α-K_xMnO_2 shows ferromagnetic and antiferromagnetic properties, respectively [19].

Density functional theory (DFT) methods facilitate the study of the electronic properties of materials. However, in some cases, such as for materials containing transition-metal oxides, the performance of standard DFT functionals is insufficient [20]. To better understand the electronic structure of materials, a variety of exchange-correlation functionals have been used. One such method is the Tran and Blaha modified Becke–Johnson exchange potential (TB-mBJ) [21] which yields a band-gap as accurate as the expensive GW method [22].

In the present study, the electronic structure and thermoelectric properties of $K_{1.33}Mn_8O_{16}$ in the bulk as well as in nanosheet structures are computed in order to investigate the potential use of materials based on $K_{1.33}Mn_8O_{16}$ as cathodes and electrocatalysts. Although there exist a few studies on the electronic structure of $K_{1.33}Mn_8O_{16}$ as a bulk material [16], to the best of our knowledge no attempt has been made to calculate the electronic properties of nanosheets, as well as the thermoelectric properties in the bulk and in nanosheet structures. In this work, the electronic properties of bulk and nanosheet of $K_{1.33}Mn_8O_{16}$ are investigated using DFT methods. Thermoelectric properties studies have been carried out using TB-mBJ that has sufficient accuracy for the prediction of the precise band gaps.

Table 1
Calculated and experimental values of Mn–O Bonds length (Å) in bulk and nanosheet structures of $K_{1.33}Mn_8O_{16}$.

Structure	Mn–O1	Mn–O2	Mn–O3	Mn–O4
Bulk	1.966	1.897	1.875	1.950
Nanosheet	1.858	1.787	1.786	1.846
Experimental	1.952	1.892	1.905	1.931

2. Methods

The electronic structure calculations of bulk and nanosheet $K_{1.33}Mn_8O_{16}$ were carried out using the full-potential linearized augmented plane wave approach for solving Kohn-Sham equations as implemented in the WIEN2k package [23]. The Perdew-Burke-Ernzerhof (PBE) functional in the generalized gradient approximation (GGA) [24] was chosen for exchange and correlation. Previous studies have shown that the GGA plus Hubbard U [20], or GGA+U method accurately predicts the ground state of manganese oxide, so GGA+U was also applied for calculating the self-interaction correction with the relation: $U_{eff}=U-J$ (J=0). The Hubbard parameter U was calculated using an ab initio approach [25], and the value of 4.8 eV was utilized in the calculations.

To compute thermoelectric properties, the TB-mBJ scheme was employed. The muffin tin (MT) radii of Mn, K and O were chosen to be 1.69, 1.15, 1.43 a.u., respectively. In the irreducible part of the first Brillouin zone, grids of 2×2×6 and 4×4×12 special k-points were used for the investigation of electronic and thermoelectric properties in the bulk. For the nanosheet structure, a grid of 2×2×1 k-points was used for both the electronic and thermoelectric properties. A 13.5 Å vacuum space was applied in the z-direction in order to avoid interactions between periodic images in the nanosheet with thickness of 4.21 Å and occupancy of 0.665 for K ions. For the wave function expansion inside the muffin tin spheres, the maximum value of the quantum number l was set to 10. In the interstitial region of the unit cell, a plane wave cutoff of $R_{MT}K_{max}$=7 was adopted, where R_{MT} stands for the smallest muffin-tin radius and K_{max} is the largest reciprocal lattice vector in the plane wave expansion. The charge density was expanded in Fourier modes up to G_{max}=20 $(Ryd)^{1/2}$, and energy and charge differences of less than 0.0001 and 0.001 were required for convergence between steps. All electronic calculations were performed on both spin-down and spin-up states. Also, spin polarization calculations were taken into

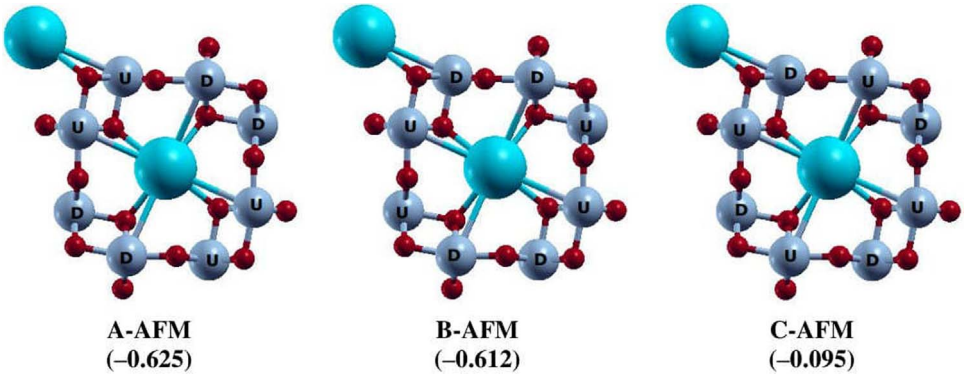

Fig. 2. The three antiferromagnetic configurations studied. The spin-up atoms are labeled as U and spin-down atoms as D. The values in parentheses show the total energies (in eV) for the structures relative to the FM state.

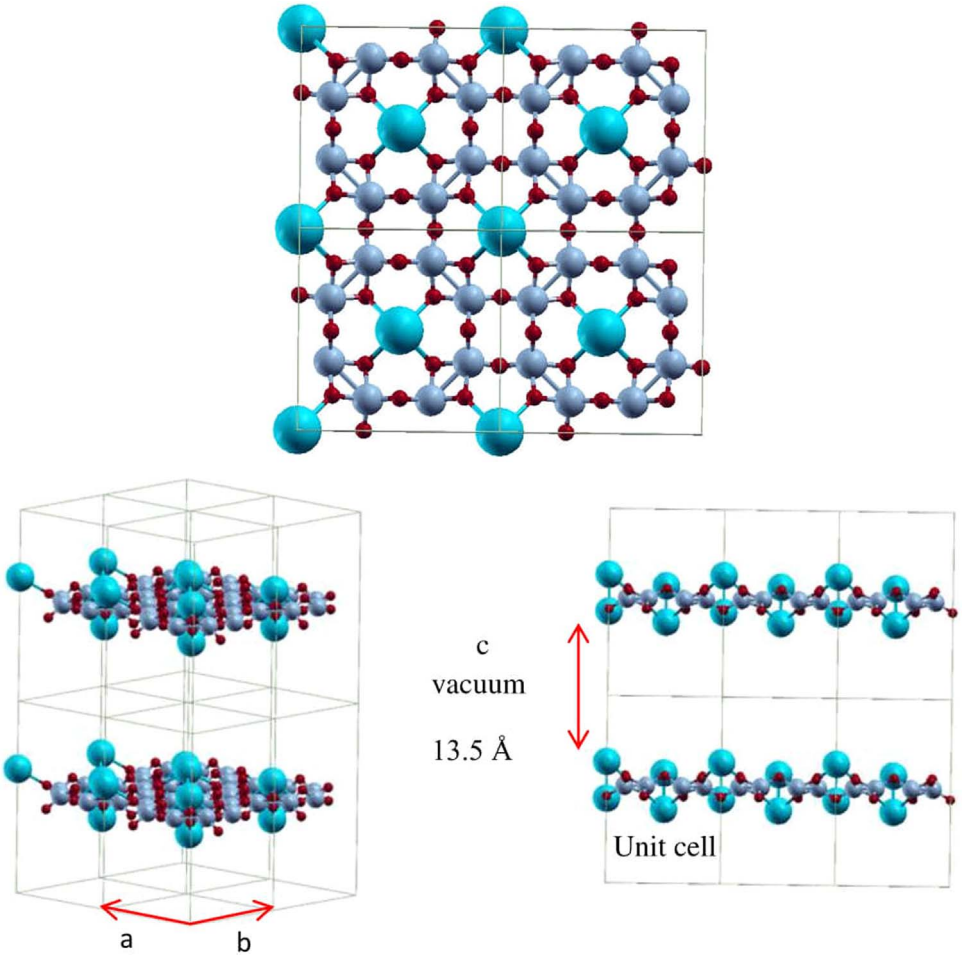

Fig. 3. Top and side views of the optimized supercell of $K_{1.33}Mn_8O_{16}$. *a*, *b* and *c* are the lattice parameters in *x*, *y* and *z* directions.

account for thermoelectric calculations. All thermo-electric computations, such as for the Seebeck coefficient, electrical conductivity, and thermal conductivity, were carried out using the BoltzTrap code [26]. Graphics are created by XCrySDen [27].

3. Results and discussion

3.1. Electronic properties

First, different magnetic configurations of Mn atoms were examined to find the ground state magnetic configuration. The possible unit cells of different magnetic patterns of Mn atoms in $K_{1.33}Mn_8O_{16}$ are shown in Figs. 1 and 2, respectively. Three different antiferromagnetic configurations, shown in Fig. 2, were chosen, as well as the ferromagnetic configuration. All magnetic structures were optimized by the GGA method. As shown in Fig. 2, the **A-AFM** configuration is the ground state magnetic configuration. The present result is in general agreement with previous studies of the magnetic structure of α-MnO_2 [18]. In the following, the ground state magnetic configuration has been utilized in the analysis.

Table 1 lists the TB-mBJ optimized bond lengths in the ground state magnetic configuration of the bulk and nanosheet $K_{1.33}Mn_8O_{16}$ structures (Fig. 3). The results indicate that there is general agreement between computational and experimental bond lengths in the bulk, whereas the bond lengths are slightly smaller in the nanosheet structure than in the bulk.

In order to calculate the electronic properties more precisely, the mBJ and GGA+*U* approximations were chosen. Calculations of the density of states (DOS) of $K_{1.33}Mn_8O_{16}$ were performed using the mBJ, GGA+*U*, and GGA approximations. The DOS, as well as the partial density of states (PDOS) projected on Mn and O atoms, are shown in Fig. 4. According to the total DOS, the bulk band gap in the TB-mBJ approximation is 1.20 ev for both spin channels. The computed band gap is larger than that computed in the GGA+*U* approximation (0.50 ev and 0.88 ev for spin-up and spin-down states, respectively) and the GGA approximation (0.55 ev and 0.50 ev for spin-up and down). The value of the band gap calculated in the TB-mBJ approximation is consistent with that predicted in other theoretical and experimental studies [16,19,28]. As shown in Fig. 4, the conduction band in all approximations has a considerable occupation at the Fermi level, and therefore, $K_{1.33}Mn_8O_{16}$ shows metallic behavior. Furthermore, according to plots of the PDOS shown in Figs. 4(b), 2*p* orbitals on Oxygen atoms have a higher population value in the valence band than in the conduction band. In addition, a strong hybridization exists between Mn 3*d* and O 2*p* orbitals in the valence band of bulk $K_{1.33}Mn_8O_{16}$. Based on the DOS plots for the orbitally resolved Mn 3*d* orbitals in Fig. 4(c) and (d), the 3*d* orbitals split into doubly-degenerate e_g orbitals ($d_{x^2-y^2}$, d_{z^2}) and triply-degenerate t_{2g} orbitals (d_{xy}, d_{xz}, d_{yz}) without any sign of Jahn-Teller distortion.

The DOS plots of the nanosheet structure are shown in Fig. 5 where notable differences between the DOS of the bulk and nanosheet structures of $K_{1.33}Mn_8O_{16}$ are observed. The $K_{1.33}Mn_8O_{16}$ nanosheet acts as an intrinsic semiconductor with a band gap of 1.3 ev (Fig. 5a), and the band gap is larger in the nanosheet than in the bulk. In bulk $K_{1.33}Mn_8O_{16}$, the Fermi level moves into the conduction band, whereas the Fermi level is located in the middle of the valence and conduction bands in the nanosheet. Moreover, as is shown in Fig. 5(b), the bonding between Mn and O atoms is due to strong hybridization between Mn 3*d*

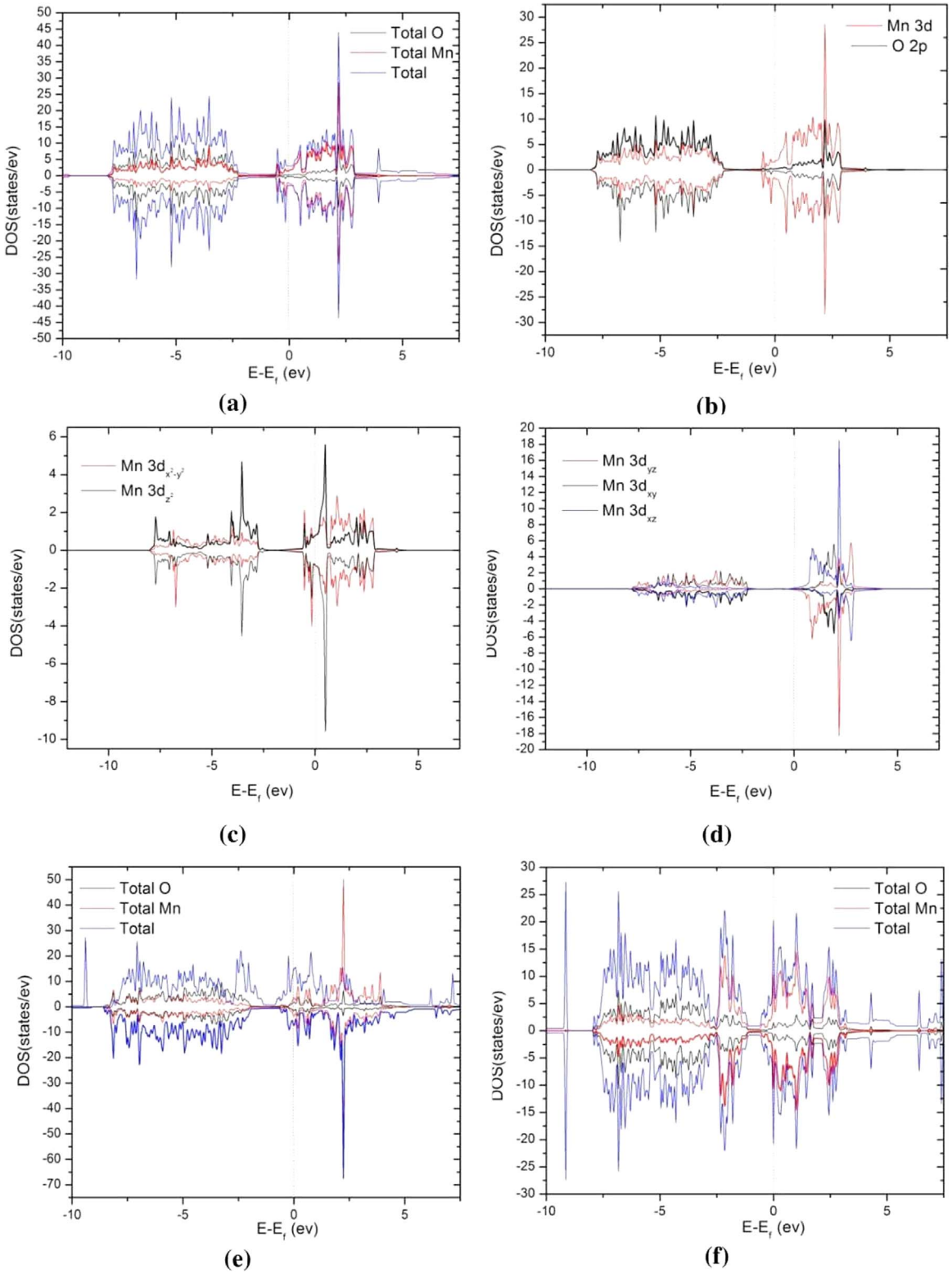

Fig. 4. Calculated DOS plots for the bulk $K_{1.33}Mn_8O_{16}$: (a) total and partial DOS, (b) partial and (c, d) orbitally resolved DOS of Mn 3*d* from TB-mBJ approximation, (e) total and partial DOS from GGA+*U* approximation, (f) total and partial DOS from GGA approximation.

and O 2*p* orbitals, similar to behavior seen in the bulk material. It should be noted that the conduction and valence bands near the Fermi level are mainly composed of Mn 3*d* orbitals while the valence band far from the Fermi level is primarily composed of O 2*p* orbitals.

It can be seen from Fig. 5(a) and (b) that the Mn 3*d* orbitals in the nanosheet behave differently than in the bulk. For a detailed study, due to various spin directions of electrons in Mn atoms (i.e., up and down), the PDOS was plotted based on the spin directions in two different groups of Mn atoms as follows: *d* orbitals of spin-up Mn atoms are shown in Fig. 5(c) and (d), while *d* orbitals of spin-down Mn atoms are shown in Fig. 5(e) and (f). There is no difference in the energy hierarchy of *d* orbitals in Fig. 5(c) and (d) and in Fig. 5(e) and (f). From Fig. 5(c) and (e), the $3d_{x^2-y^2}$ orbitals are situated in the bottom of the conduction band and the $3d_{z^2}$ orbitals are located at the top of the

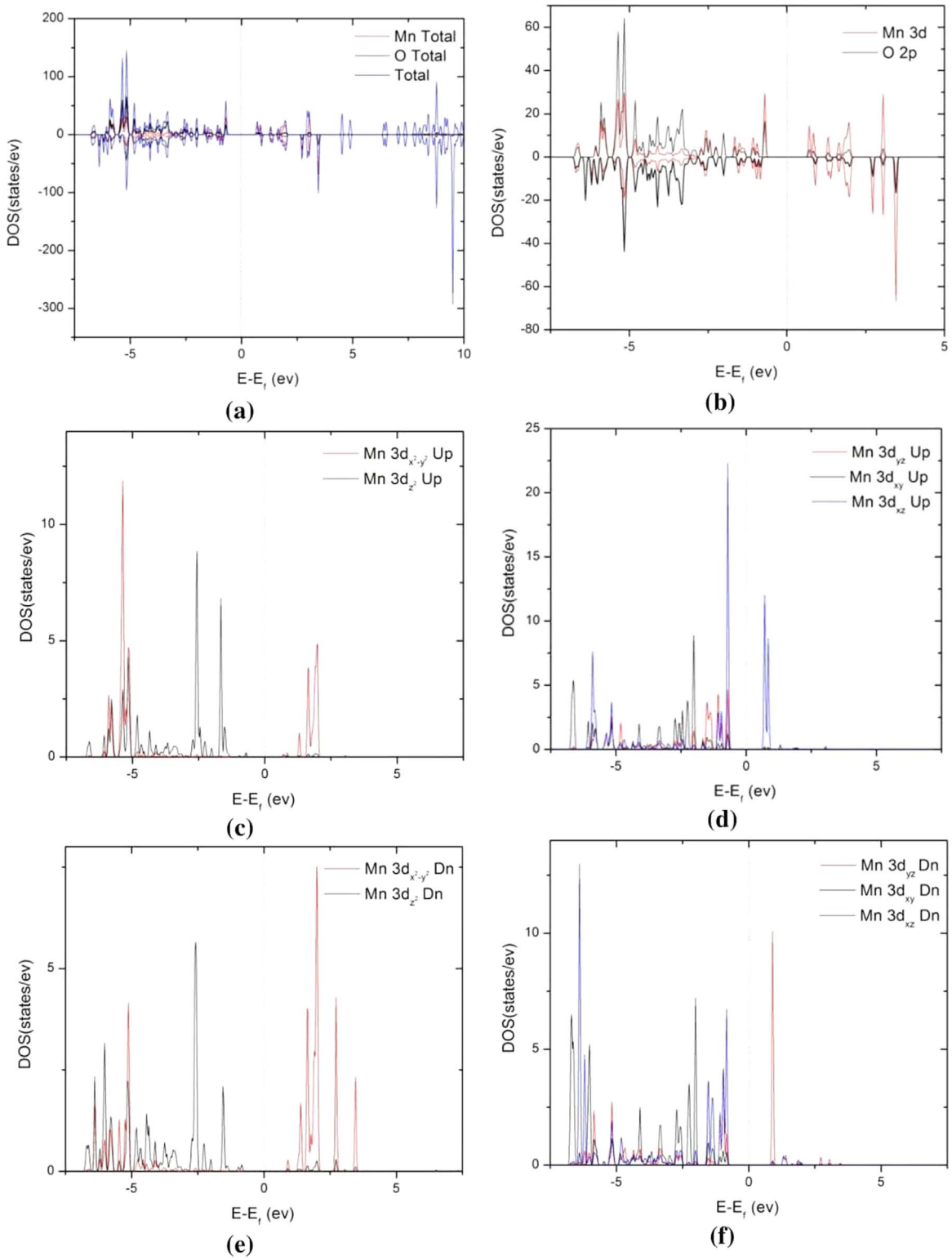

Fig. 5. Calculated DOS plots for the nanosheet $K_{1.33}Mn_8O_{16}$: (a) total and partial DOS, (b) partial and (c, d) orbitally resolved DOS of spin-up Mn atoms, and (e, f) orbitally resolved DOS of spin-down Mn atoms.

valence band. On the other hand, a comparison between Fig. 4(d) with Fig. 5(d) and (f) shows that the triple degeneracy of d_{xy}, d_{xz}, d_{yz} orbitals in the nanosheet is lifted in contrast to what is observed in the bulk. The distorted e_g orbitals split into $d_{x^2-y^2}$ and d_{z^2} orbitals, where the $d_{x^2-y^2}$ orbitals are lifted to the highest energy level and d_{z^2} orbitals are lifted to the lowest level. Moreover, t_{2g} orbitals split into d_{xy} and d_{xz},d_{yz} orbitals, d_{xy} orbitals shift to lower energy than the doubly degenerate orbitals of d_{xz},d_{yz}. This leads to a change in the oxidation number of Mn atoms. For a more detailed analysis, we have calculated the integral of PDOS up to the Fermi level, and the results are listed in Table 2. In bulk $K_{1.33}Mn_8O_{16}$, the electron configuration of $e_g^1t_{2g}^2$ is observed for all metal ions, so we have Mn^{4+} ions. In fact, In the bulk $K_{1.33}M_8O_{16}$, the ratio between Mn^{4+} and Mn^{3+} ions is very large and few Mn^{3+} ions exist [29]. In the nanosheet, there is also $e_g^1t_{2g}^3$

Table 2
Electron occupancy in d orbitals of Mn atoms in bulk[(a)] and nanosheet[(b)] $K_{1.33}Mn_8O_{16}$. The values in brackets represent another set of electron occupancy in d_{xz} and d_{yz} orbitals in fifty percent of Mn^{4+} ions.

	d	$d_{x^2-y^2}$	d_{z^2}	d_{xz}	d_{yz}	d_{xy}
$Mn^{4+(a)}$	3.09	0.40	0.73	0.23 (0.87)	0.87)0.23)	0.86
$Mn^{4+(b)}$	3.09	0.29	0.82	0.26 (0.85)	0.85 (0.26)	0.86
$Mn^{3+(b)}$	3.55	0.25	0.83	0.81	0.80	0.85

configuration for some ions, so both Mn^{4+} and Mn^{3+} ions can be found in the nanosheet. Despite having some ions with lower oxidation number, no obvious sign of a Jahn-Teller distortion can be observed in the structural parameters of the nanosheet, which demonstrates the partial reduction of Mn^{4+} to Mn^{3+}. Similar behavior has been observed for the cryptomelane (α-MnO_2) polymorph electrodes using XRD patterns [30].

The authors of [31,32] suggest that the number of e_g electrons plays an important role in OER. In fact, in transition metal oxides (TMOs) which have populations of e_g electrons close to unity, the TMO displays high catalytic activity in the OER because e_g electrons can forms σ bonds with oxygen more easily than in t_{2g} orbitals. The findings of the current study suggest that both the nanosheet and bulk $K_{1.33}Mn_8O_{16}$ have a high activity in OER and ORR.

To compare the catalytic activity of nanosheet and bulk of $K_{1.33}Mn_8O_{16}$ structures, the O p-band center descriptor has been also used [33,34]. This descriptor can predict the catalytic activity in the transition metal oxide $K_{1.33}Mn_8O_{16}$. The O p-band center relative to the Fermi level is calculated according to the equation:

$$\varepsilon_p = \frac{\int_{-\infty}^{E_f} E\rho_p EdE}{\int_{-\infty}^{E_f} \rho_p EdE} \quad (1)$$

In this equation, ρ_p is the density of states projected onto atomic oxygen p bands and E_f is the energy of the Fermi level. The O p-band center of the nanosheet structure is closer to the Fermi level (−4.29 eV for the spin-up and −4.34 eV for the spin-down) compared to the bulk value (−4.94 eV for spin-up and −4.98 eV for spin-down), as is evident in Fig. 6. This implies that the nanosheet $K_{1.33}Mn_8O_{16}$ has higher catalytic activity than the bulk $K_{1.33}Mn_8O_{16}$. Here, we turn to detailed band structure analysis of the bulk and nanosheet of $K_{1.33}Mn_8O_{16}$. The primitive first Brillouin zone and electronic band structures of bulk and nanosheet $K_{1.33}Mn_8O_{16}$ are shown in Fig. 7. According to these figures, the bulk of $K_{1.33}Mn_8O_{16}$ exhibits metallic character at the Γ-Z symmetry point of the Brillouin zone, while the nanosheet structure shows semiconducting character with a direct band gap. All presented band structures are in agreement with the TDOS data. The band structures for the spin-up and spin-down states do not display any significant differences.

In addition, according to Fig. 8, the Fermi surface consists of six bands which cross the Fermi level around the Γ-Z lines, which is mainly associated with the Mn d orbitals. All of these sheets are characterized by hole bands which are mostly from $d_{x^2-y^2}$, d_{z^2} orbitals.

3.2. Thermoelectric calculation

3.2.1. Seebeck coefficient

One important property in thermoelectricity is the Seebeck coefficient, which determines the induced voltage that arises due to a given temperature difference [26]:

$$S = \frac{\Delta V}{\Delta T}. \quad (2)$$

The calculated Seebeck coefficients for bulk and nanosheet $K_{1.33}Mn_8O_{16}$ as a function of the chemical potential are presented in Fig. 9 at 300, 500, and 800 K for both spin channels. According to Fig. 9(a) and (b), it can be inferred that the Seebeck coefficient of bulk $K_{1.33}Mn_8O_{16}$ is very small around the Fermi level. The maximum values of the Seebeck coefficient at different temperatures for the bulk $K_{1.33}Mn_8O_{16}$ are computed to be 855.5, 469.3 μV/K both at the chemical potential of −1.59, and 267.9 μV/K at the chemical potential of −1.63 ev at 300 K, 500 K, and 800 K, respectively. On the other hand, it can be seen that there are no sharp peaks for positive chemical potentials. Therefore, it can be concluded that the Seebeck coefficient has a maximum value at 300 K and decreases with increasing the temperature. As shown in Fig. 9(a) and (b), the behavior of the Seebeck coefficients as a function of chemical potential for the bulk $K_{1.33}Mn_8O_{16}$ is similar in both spin channels but with slight differences in absolute values. Bulk $K_{1.33}Mn_8O_{16}$ shows metallic-like behavior, so it displays a lower absolute value of the Seebeck coefficient compared to the semiconductor $K_{1.33}Mn_8O_{16}$ nanosheet. In metals, owing to equivalent contributions of electrons and holes to induce thermoelectric voltage, they cancel each other's contribution and the resulting induced voltage is small.

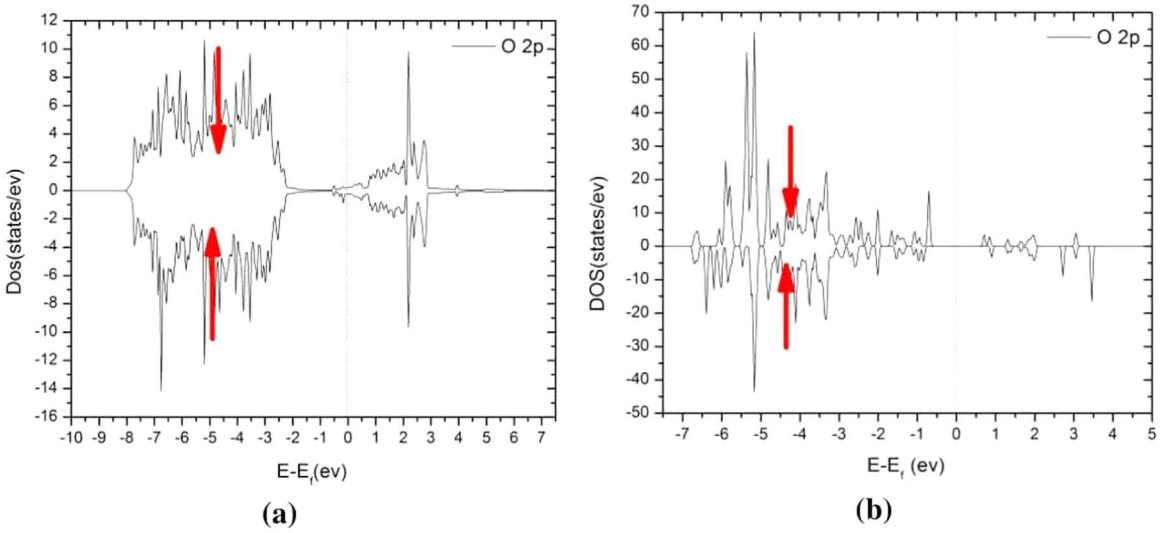

Fig. 6. Projected p band states of $K_{1.33}Mn_8O_{16}$ in (a) bulk and (b) nanosheet; the p band center is marked by red arrows. (For interpretation of the references to color in this figure legend, the reader is referred to the web version of this article).

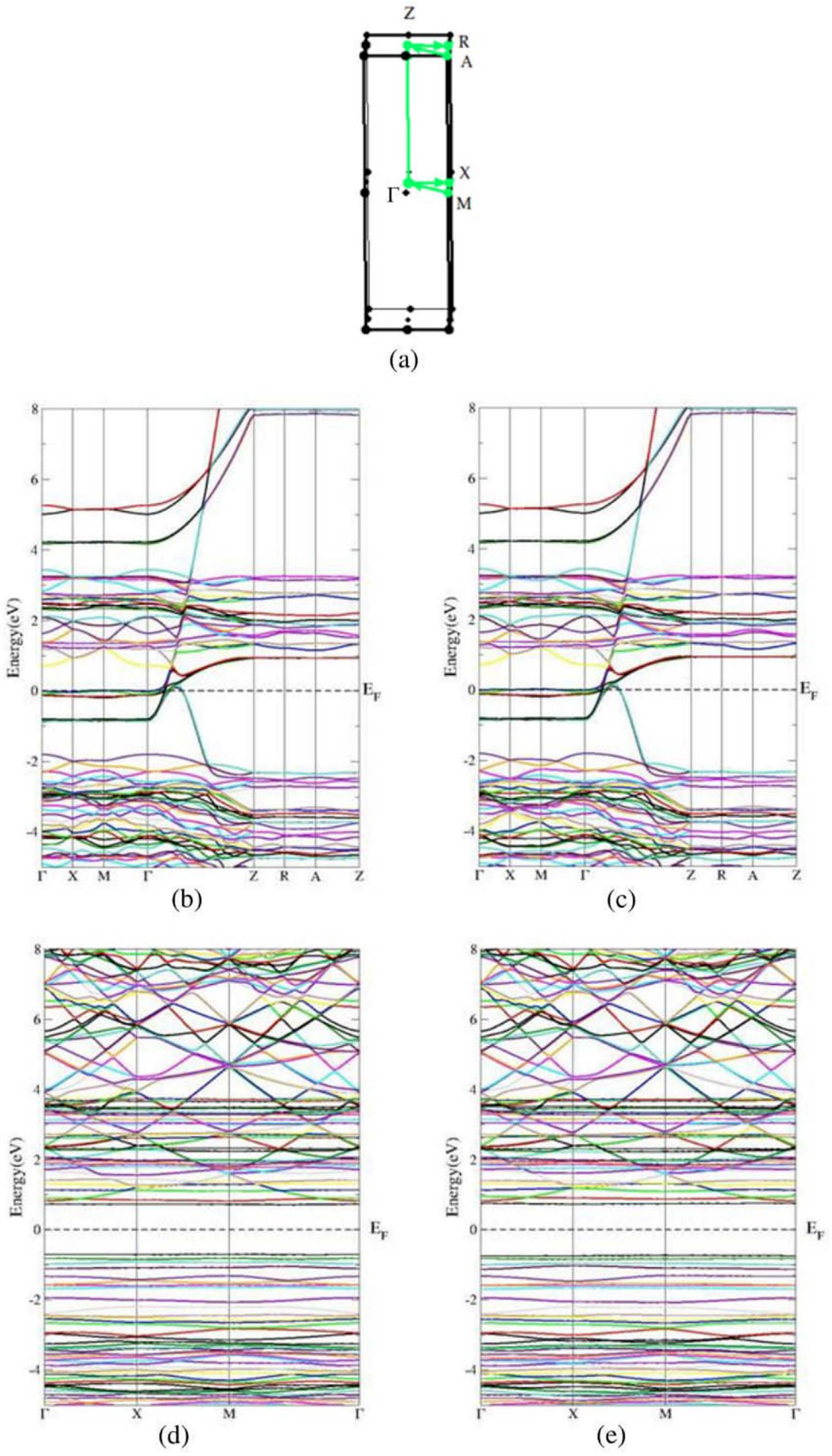

Fig. 7. Primitive first Brillouin zone of $K_{1.33}Mn_8O_{16}$ (a), electronic band structures of bulk $K_{1.33}Mn_8O_{16}$ for the (b) spin-up and (c) spin-down states, and the band structures for the $K_{1.33}Mn_8O_{16}$ nanosheet for (d) spin-up and (e) spin-down states.

Fig. 8. fm surface in the first Brillouin zone of bulk $K_{1.33}Mn_8O_{16}$.

In the nanosheet, the maximum absolute value of the Seebeck coefficient is about 2154 μV/K for an n-type (positive chemical potential) material around the Fermi level, but for the p-type (negative chemical potential) case, it decreases to 2063 μV/K at 300 K in the spin-up channel. On the other hand, for the spin-down channel, the corresponding peaks rise to 2235 μV/K for the p-type and 2236 μV/K for an n-type material. From the Fig. 9(c) and (d), it can be seen that at high temperatures (500 K and 800 K), smaller values of Seebeck coefficient are obtained than at 300 K. We can aslo compare the thermoelectric power of the $K_{1.33}Mn_8O_{16}$ nanosheet with $SrTiO_3$, SnO_2 and silicide materials such as Mg_2Si. $SrTiO_3$ functions as a catalyst and silicide [35] and SnO_2 have high performances in power generation. These materials have some advantages similar to $K_{1.33}Mn_8O_{16}$ including low-cost and environmental friendliness. The maximum values of seebeck coefficients in $SrTiO_3$ [36] and Sb-doped SnO_2 [37] and Mg_2Si [38] are approximately 300, 800 and 1000 μV/K at 300 K at the Fermi level which are pale in comparison to the nanosheet of $K_{1.33}Mn_8O_{16}$ material. In addition, the Seebeck coefficients of these materials decrease with increasing the temperature.

3.2.2. Electrical conductivity

Another important parameter that can help in the evaluation of the thermoelectric performance of a material is its electrical conductivity. In bulk and nanosheet $K_{1.33}Mn_8O_{16}$ structures, the electrical conductivity parameter is evaluated at 300 K as follow [26]:

$$\sigma_{\alpha\beta}(T;\mu) = \frac{1}{\Omega}\int \sigma_{\alpha\beta}(\varepsilon)\left[-\frac{\partial f_\mu(T;\varepsilon)}{\partial \varepsilon}\right]d\varepsilon, \quad (3)$$

where Ω denotes the volume of the unit cell, and f is the Fermi-Dirac distribution function. As shown in Fig. 10(a), the maximum value of electrical conductivity of the bulk structure is 490 (10^{18} 1/mΩs) which is located at the chemical potential of −1.0 eV. Fig. 10(a) also shows that the maximum value of electrical conductivity of the spin-down channel is similar to that of the spin-up channel. In contrast, as Fig. 10(b) shows, the electrical conductivity of the nanosheet is zero at the Fermi level and increases with an increase in the chemical potential towards 0.5 eV. The increase in electrical conductivity continues up to 1.5 (10^{18} 1/mΩs) at 300 K for the spin-up channel. This maximum value is identified at the chemical potential of −1.5 eV. In contrast to the identical situation of spin-up and spin-down channels in bulk $K_{1.33}Mn_8O_{16}$, two different spin channels in the nanosheet of $K_{1.33}Mn_8O_{16}$ exhibit different absolute values of electrical conductivity. The spin-up channel has a higher value of electrical conductivity than the spin-down channel.

3.2.3. Thermal conductivity

Thermal conductivity values at 300 K were calculated for the spin up and down channels. According to Fig. 11(a), the thermal conductivity of bulk $K_{1.33}Mn_8O_{16}$ starts to increase at the value of the chemical potential of −0.5 ev and reaches a maximum value of 2.75 (10^{15} W/mks) at a value of −1.0 eV, then decreases to zero at the chemical potential of −1.4 eV. In addition, it is clear from Fig. 11(a) that there exists no crucial difference between spin up and spin down channels. On the other hand, the thermal conductivity of the nanosheet in Fig. 11(b) has a value of zero at the Fermi level. Furthermore, the thermal conductivity increases at a value of the chemical potential of −0.5 eV and reaches its peak value of 0.007 (10^{15} W/mks) at −1.3 eV for the spin-up channel. From the findings of the thermal conductivity, it can be suggested that the supercell of $K_{1.33}Mn_8O_{16}$ has a notably lower value compared with that seen in bulk.

The capability of power generators is related to the magnitude of the figure of merit ZT [39,40] defined by the equation $ZT=S^2\sigma T/\kappa$, where S stands for the Seebeck coefficient, κ is the thermal conductivity, σ is the electrical conductivity and T is temperature. Figures of merit are studied and shown in Fig. 12 as a function of chemical potential. The value of figure of merit for the nanosheet is approximately 1 at the Fermi level, while a lower value of 0.5 is observed in bulk $K_{1.33}Mn_8O_{16}$ around the Fermi level. All findings from the Figs. 9–12 suggest the potential of the nanosheet of $K_{1.33}Mn_8O_{16}$ to act as a power generation device due to having a larger value of ZT.

4. Conclusions

In summary, the electronic and thermoelectric properties of bulk and nanosheet structures of $K_{1.33}Mn_8O_{16}$ were investigated using density functional theory methods. For a better understanding of the thermoelectric properties, the TB-mBJ exchange-correlation potential was applied. The results indicate that the presence of the John-Teller distortion in the nanosheet of $K_{1.33}Mn_8O_{16}$ leads to a distortion in the density of states. High electrocatalytic activity in nanosheet exists not only because of the presence of one electron in an e_g orbital, but also due to the closer location of the O p-band center to the Fermi level. Moreover, a high Seebeck coefficient is observed for the nanosheet. Furthermore, this study shows that the nanosheet of $K_{1.33}Mn_8O_{16}$ has a lower thermal conductivity compared to the bulk $K_{1.33}Mn_8O_{16}$ and unlike the bulk structure, the figure of merit is approximately 1 at room temperature in the nanosheet. Therefore, the nanosheet structure is a good candidate for a cathode material in fuel cell and batteries. As a further study, it would be interesting to assess the effect of doping transition metals, such as Co, in the bulk $K_{1.33}Mn_8O_{16}$ and compare the activity of bulk $K_{1.33}Mn_8O_{16}$ with that of the nanosheet.

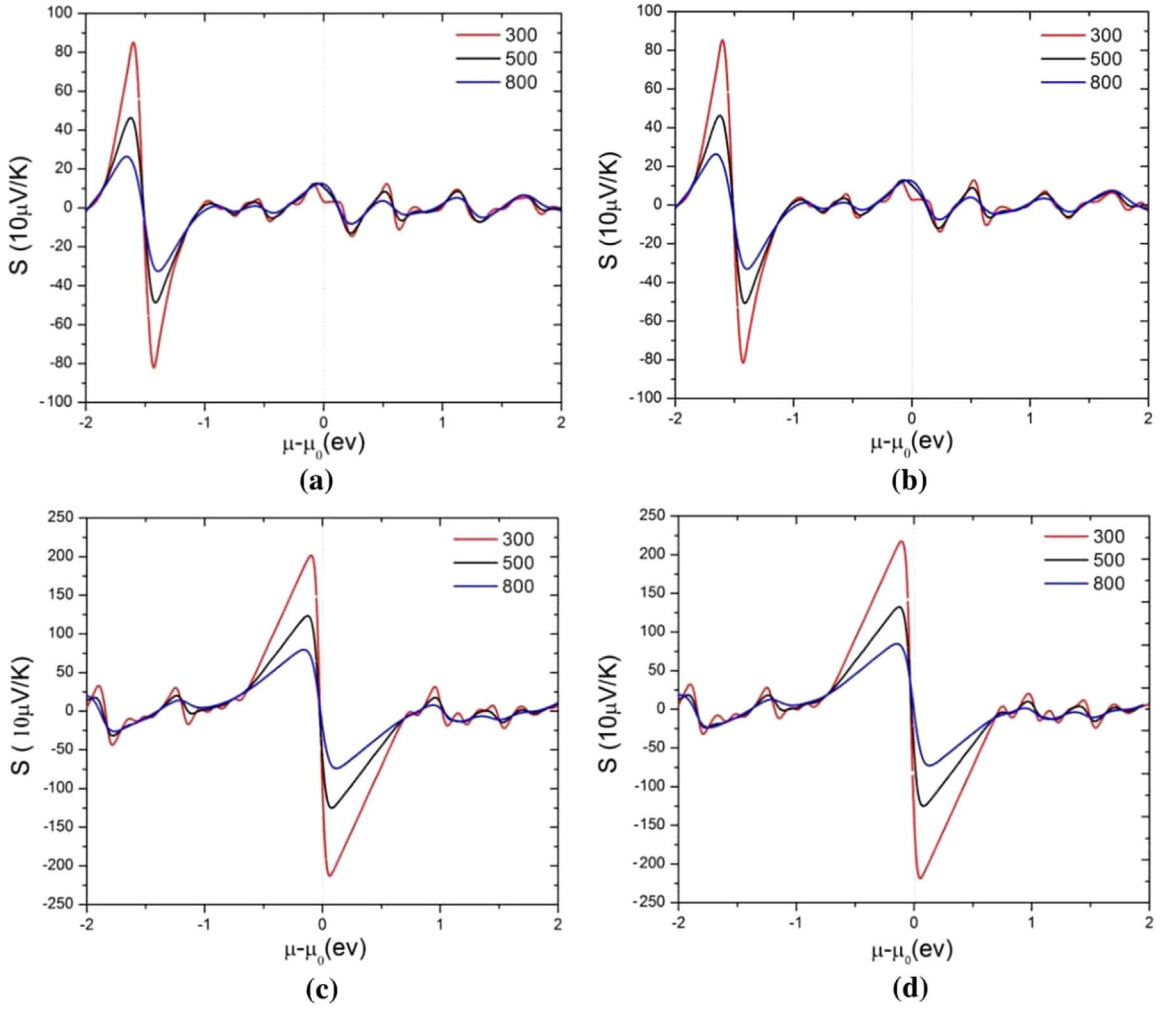

Fig. 9. Calculated Seebeck coefficient vs. the chemical potential for (a) the spin-up bulk, (b) the spin-down bulk, (c) the spin-up nanosheet, (d) the spin-down nanosheet at 300, 500 and 800 K temperatures.

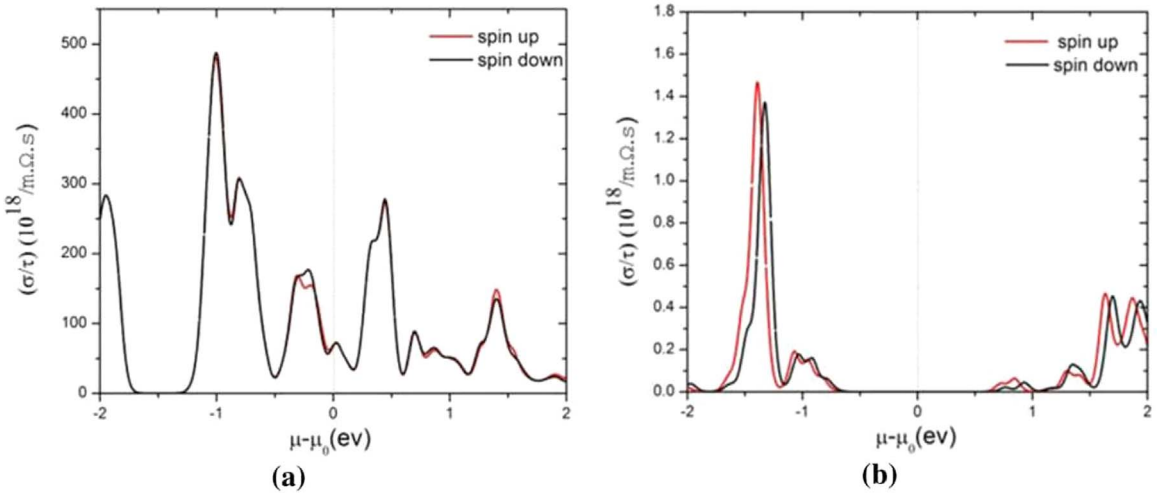

Fig. 10. Calculated electrical conductivity vs. chemical potential at 300 K in both spin directions for (a) the bulk and (b) the nanosheet of $K_{1.33}Mn_8O_{16}$.

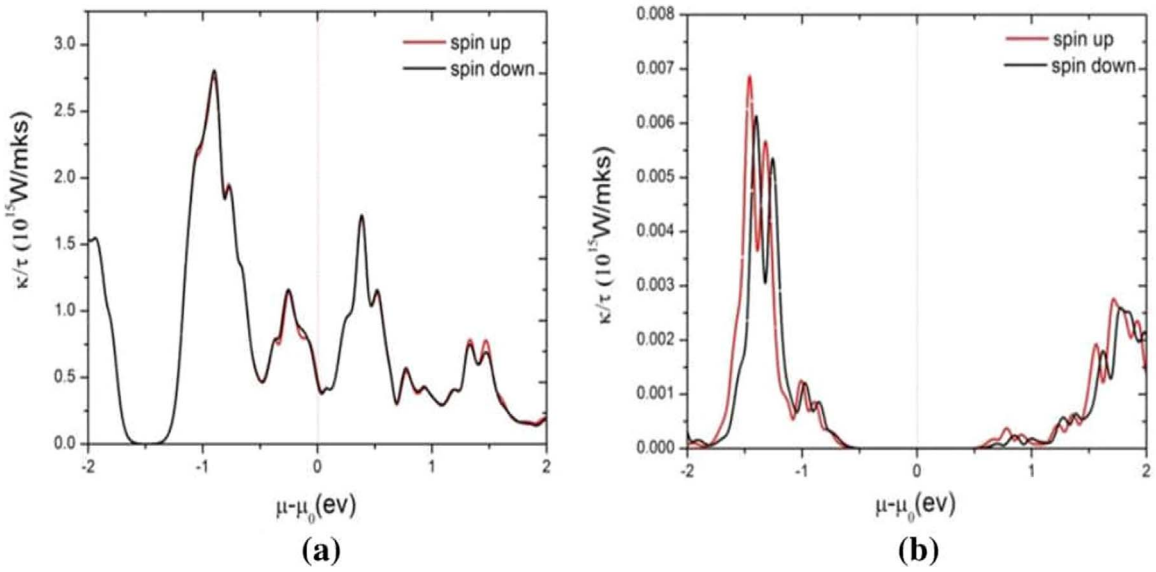

Fig. 11. Calculated thermal conductivity vs. chemical potential at 300 K in both spin directions for (a) the bulk and (b) the nanosheet of $K_{1.33}Mn_8O_{16}$.

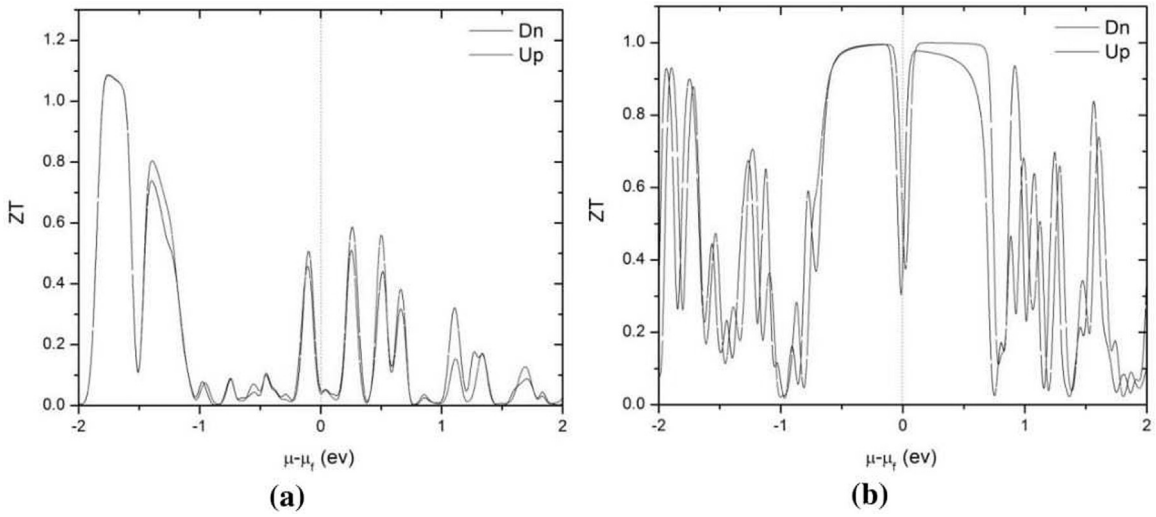

Fig. 12. Calculated figure of merit as a function of the chemical potential at 300 K for both spin channel in (a) bulk and (b) nanosheet of $K_{1.33}Mn_8O_{16}$.

Appendix A. Supplementary material

Supplementary data associated with this article can be found in the online version at http://dx.doi.org/10.1016/j.jssc.2016.12.009.

References

[1] L. Jorissen, J. Power Sour. 155 (2006) 23.
[2] V. Nikolova, J. Power Sour. 185 (2008) 727.
[3] B. Sajdl, K. Micka, P. Krtil, et al., Electrochim. Acta 40 (1995) 2005.
[4] X. Han, et al., Nano Res. 8 (2015) 156.
[5] A. Yu, H. Woong Park, A. Davies, D.C. Higgins, Z. Chen, X. Xiao, J. Phys. Chem. Lett. 2 (2011) 1855.
[6] A. Aziznia, C.W. Oloman, E.L. Gyenge, J. Power Sour. 212 (2012) 154.
[7] D. Zhai, et al., J. Power Sour. 196 (2011) 7860.
[8] P. Hosseini Benhangi, A. Alfantazi, E. Gyenge, Electrochim. Acta 123 (2014) 42–50.
[9] C. Zang, et al., RSC Adv. 2 (2012) 1643.
[10] Y. Meng, W. Song, H. Huang, Z. Ren, S. Chen, S.L. Suib, J. Am. Chem. Soc. 136 (2014) 11452.
[11] T. Wei, Y. Huang, L. Jiang, J. Yang, R. Zeng, J.B. Goodenough, RSC Adv. 3 (2013) 2336.
[12] K. Selvakumar, S.M.S. Kumar, R. Thangamuthu, G. Kruthika, P. Murugan, Int. J. Hydrog. Energy 39 (2014) 21024.
[13] J. Zhu, et al., J. Mater. Chem. A 1 (2013) 8154.
[14] Y. Yuan, et al., Nano Lett. 15 (2015) 2998.
[15] W.K. pang, V.K. Peterson, N. Sharma, C. Zhang, Z. Guo, J. Phys. Chem. C 118 (2014), 2014, p. 3976.
[16] E. Cockayne, L. Li, Chem. Phys. Lett. 544 (2012) 53.
[17] D.A. Kitchaev, H. Peng, Y. Liu, J. Sun, J.P. Perdew, G. Ceder, Phys. Rev. B 93 (2016) 045132.
[18] Y. Crespo, N. Seriani, Phys. Rev. B 88 (2013) 144428.
[19] L. Tseng, et al., Sci. Rep. 5 (2015) 9094.
[20] V.L. Anisimov, J. Zaanen, O.K. Anderson, Phys. Rev. B 44 (1991) 943.
[21] F. Tran, P. Blaha, Phys. Rev. Lett. 102 (2009) 226401.
[22] L. Hedin, Phys. Rev. 139 (3A) (1965) A796.
[23] P.Blaha, K.Schwarz, G.K.H.Madsen, D.Kvasnicka, J.Luitz, Wien2k. An augmented plane wave+ local orbitals program for calculating crystal properties, 2001.
[24] J.P. Perdew, K. Burke, M. Ernzerhof, Phys. Rev. Lett. 77 (1996) 3865.
[25] G. Madsen, P. Novak, WIEN2k-Textb. (2007).
[26] G.K.H. Madsen, D.J. Singh, Comput. Phys. Commun. 175 (2006) 67.
[27] A. Kokalj, Comput. Mater. Sci. 28 (2003) 155.
[28] T. Gao, M. Glerup, F. Krumeich, R. Nesper, H. Fjellvag, P. Norby, J. Phys. Chem. C 112 (2008) 13134.
[29] B.N. Deguzman, et al., Chem. Mater. 6 (1994) 815.
[30] H.A. Pan, et al., J. Electrochem. Soc. 162 (2015) A5106.

[31] J. Suntivich, K.J. May, H.A. Gasteiger, J.B. Goodenough, Y. Shao-Horn, Sci. Rep. 334 (2011) 1383.
[32] U. Maitra, B.S. Naidu, A. Govindaraj, C.N.R. Rao, Proc. Natl. Acad. Sci. USA 110 (2013) 11704.
[33] A. Grimaud, et al., Nat. Commun. 4 (2013).
[34] Y.L. Lee, et al., Energy Environ. Sci. 4 (2011) 3966.
[35] V.K. Zaitsev, M.I. Fedorov, E.A. Gurieva, I.S. Eremin, P.P. Konstantinov, A. Yu, Samunin, M.V. Vedernikov, Phys. Rev. B 74 (2006) 045207.
[36] A.H. Reshak, Renew. Energy 76 (2015) 36.
[37] P.D. Borges, et al., J. Solid State Chem. 231 (2015) 123.
[38] G. Murtaza, et al., Mater. Sci. Semicond. Process. 40 (2015) 429.
[39] A.I. Hochbaum, et al., Nature 451 (2008) 163.
[40] G.J. Snyder, E.S. Toberer, Nat. Mater. 7 (2008) 105.